Sensors & Actuators: A. Physical 338 (2022) 113496

Contents lists available at ScienceDirect

Sensors and Actuators: A. Physical

journal homepage: www.journals.elsevier.com/sensors-and-actuators-a-physical

Simultaneous tip force and displacement sensing for AFM cantilevers with on-chip actuation: Design and characterization for off-resonance tapping mode

Natã F.S. de Bem [a,*], Michael G. Ruppert [a], Andrew J. Fleming [a], Yuen K. Yong [a]

[a] University of Newcastle, Callaghan, NSW 2308, Australia

ARTICLE INFO

Keywords:
Active cantilever
Dual-sensing
Atomic force microscopy
Tip force

ABSTRACT

The use of integrated on-chip actuation simplifies the identification of a cantilever resonance, can improve imaging speed, and enables the use of smaller cantilevers, which is required for low-force imaging at high speed. This article describes a cantilever with on-chip actuation and novel dual-sensing capabilities for AFM. The dual-sensing configuration allows for tip displacement and tip force to be measured simultaneously. A mathematical model is developed and validated with finite element analysis. A physical prototype is presented, and its calibration and validation are presented. The cantilever is optimized for use in off-resonance tapping modes. Experimental results demonstrate an agreement between the on-chip sensors and external force and displacement measurements.

1. Introduction

The atomic force microscope (AFM) [1] provides unique capabilities for imaging the structure and physical properties of surfaces, such as chemical composition [2], electrical characteristics [3], stiffness [4], and topography [5,6].

The operating mode of an AFM describes the conditions which are held constant, e.g. the contact force; the measured signal, e.g. the deflection; and the cantilever excitation that may exist in dynamic modes such as intermittent contact mode. The most commonly used modes include constant-force contact mode [7], and constant-amplitude intermittent-contact mode [7–9]. More recently, the demand for low tip-sample interaction forces has motivated the development of off-resonance tapping (ORT) modes [7,8,10].

Unlike the constant-amplitude intermittent contact mode, ORT excites the cantilever at a frequency well below its resonance [11–14], which eliminates the complexities of working at the resonance frequency [15]. Due to the low frequency of cantilever excitation in ORT modes, the cantilever can be modeled as quasistatic, where the stiffness rather than the mass dominates its response [13].

In ORT, force-distance curves are generated at each cycle as the tip approaches and retracts from the sample. Typically, the maximum interaction force is the controlled parameter, which allows direct limitation of the forces acting between the tip and sample [15]. The capability to directly limit the tip-sample force is particularly advantageous when imaging soft and fragile samples [10–12], including in liquid environments [13].

The concept of the atomic force microscope has been largely unaltered since it was conceived. The AFM is composed of a microcantilever with a sharp tip that is moved over the sample by a vertical nanopositioner [16–19]. The cantilever undergoes deflections due to the interatomic forces acting on its tip. These deflections can be related to the characteristics of the sample, such as its topography. An optical beam deflection (OBD) system is used to identify the deflection [5,20]. The OBD system is composed of a light beam focused on the cantilever's free-end and reflected onto a photodiode [16,19]. The OBD system is calibrated such that the motion of the cantilever's tip causes the beam to change its position on the photodiode [5,9,21–23].

In all of the imaging modes discussed thus far, where the cantilever deflection is controlled, the imaging speed is typically limited by the bandwidth of the vertical nanopositioner, which moves the vertical position of the cantilever relative to the sample [8,39–41]. This vertical positioning bandwidth is typically a few hundred Hertz in microscopes with a vertical range on the order of 50μm (Table 1). This limitation restricts the scanning rate to approximately 1–10 lines per second, and the imaging period to 25–250 s (for a 256×256 pixel image). However,

* Corresponding author.
E-mail address: Natan.Franco@uon.edu.au (N.F.S. Bem).

https://doi.org/10.1016/j.sna.2022.113496
Received 2 September 2021; Received in revised form 13 February 2022; Accepted 3 March 2022
Available online 8 March 2022
0924-4247/© 2022 Elsevier B.V. All rights reserved.

Table 1
Comparison of travel range and resonance frequency for different motion techniques commonly used in AFMs. The vertical positioner and piezo shaker were measured from the Nanosurf AFM [24], while the direct actuation was measured from the cantilever showed in this work.

Motion method	Range	Res. Frequency
Vertical positioner	$\pm 50\mu$ m	200 Hz
Piezo shaker	± 2 nm	10 kHz
Direct actuation	± 150 nm	< 15 kHz

there is significant demand for faster imaging speeds to enable the study of rapidly-changing phenomena, especially in living organisms and bio-molecular imaging [42–45].

An alternative to the low bandwidth of the vertical nanopositioner is base excitation. In this method, a piezoelectric chip (piezo shaker) excites the cantilever [46–48]. As the name suggests, the excitation occurs at the base of the cantilever chip. Base excitation is used for imaging modes modes that operate at, or near, the resonance frequency of the cantilever. Since the travel range of the base excitation chip is usually less than $\pm$ 10 nm for low frequencies, this cannot be used for ORT.

Direct actuation of the cantilever is an alternative method that minimizes the coupling between the cantilever and structural resonances of the scanner and microscope. The most studied methods for direct cantilever actuation are piezoelectric actuation [35], photothermal excitation using a focused laser beam [32,49,50], magnetic [28], and electrothermal actuation [26,27]. Table 2 shows a summary of each technique. All four techniques can be used for on-resonance or off-resonance modes. Electrothermal excitation (AN200, Anasys Instruments), magnetically driven cantilevers (iDrive, Asylum Instruments), and photothermal excitation (CleanDrive, Nanosurf) are available commercially [28,51,52]. However, only electrothermal and piezoelectric cantilevers are compatible with MEMS integration. Both photothermal and magnetic drive require an external source to drive the cantilever (a laser or a coil for photothermal and magnetic driven cantilevers). With the exception of electrothermal actuation, the other three methods display a fast response time [36,38,53,54], making them suitable for high-speed microscopy.

In photothermal excitation, the laser beam is focused onto a location near the base of the cantilever to induce bending due the temperature difference between the top and bottom surfaces [11,14,32–34]. However, similar to base excitation, photothermal actuation is best suited to excitation of the resonance due to the small actuation force [55]. Furthermore, the induced heat on the cantilever can damage sensitive samples [55] and causes this technique to be incompatible with integrated sensing.

Electrothermal actuation uses a microheater on a bimorph or trimorph cantilever [25,25,26]. As the heat dissipates, it induces mechanical stress in the cantilever, leading to bending [25,26,56]. Similar to photothermal actuation, the induced high temperature tends to damage sensitive samples [57]. While it shows a large displacement with low applied voltages, the response is slow compared to photothermal, piezoelectric and magnetic driven cantilevers [53].

Magnetically-driven cantilevers for AFM typically consist of a magnetic bead or particle attached to the top surface close to its free-end [30,31,58]. The bead or particle is exposed to a magnetic field, generated by a coil or a magnet, which causes the cantilever to undergo a displacement [28,29]. However, magnetically-driven cantilever faces limitations such as stability issues recurring from the demanding stability control and output voltage range in the coil. These limitations become more severe as the cantilever size is reduced [29]. Magnetically-driven cantilevers also have reproducibility limitations related to the varying geometry and magnetic properties of the magnets used in the cantilevers [59].

Piezoelectric on-chip cantilever actuation is an alternative to photothermal and electrothermal actuation that does not result in heating [15,37] or requires a magnetic cantilever, with speeds that surpass the standard piezotube [36]. Piezoelectric on-cip actuation also allows for parallel scanning [35]. This technique can be used at the resonance frequency or outside it, as large deflections are possible by increasing the applied voltage at the actuator (Table 1). Direct piezoelectric on-chip actuation also offers the benefit of being compatible with MEMS (microelectromechanical systems) fabrication processes.

Smaller cantilevers provide the advantage of faster scans and higher force sensitivity [60,61], meaning that softer samples and less invasive imaging is performed in conjunction with higher scanning rates [62].

Aside from the issues with cantilever excitation, there are also limitations on the minimum cantilever width, which arise from the optical beam deflection (OBD) system. Since the OBD system uses a collimated laser beam, the cantilever area must be large enough to deflect a significant percentage of the beam. To reduce the beam diameter, focusing lenses can be employed, but this significantly increases complexity [23] and complicates the beam alignment.

Integrated sensing has been reported as a substitute for the OBD system [5]. Piezoelectric [63,64] and piezoresistive [35,49,65] sensors have been shown to be suitable for integrated sensing, with the latter being commercially available [35]. Currently, integrated sensing has a higher noise density compared to the best OBD systems [66]. Still, it offers the possibility of parallel imaging, and imaging in environments with low or varying light conditions and light-sensitive samples [5]. Alike piezoelectric actuation, integrated piezoelectric sensors are compatible with MEMS fabrication processes, can be made of the same material as the actuator [63], and are also compatible with the miniaturization of the cantilever [37].

The inclusion of both on-chip actuation and sensing combines the advantages of both techniques, allowing smaller cantilevers and higher operating frequencies. However, due to the close proximity of the actuator and sensor, cross-coupling arises in the sensor's response [67,68]. A major disadvantage is that the measured deflection now includes both the deflection due to actuation, and the deflection resulting from tip-sample interaction.

This article presents a cantilever system composed of on-chip actuation and dual on-chip sensors. The second sensor allows both the total deflection of the cantilever and the tip-sample interaction force to be directly measured. The proposed sensors are piezoelectric which are not suited to static contact modes but are ideal for off-resonance dynamic modes, such as ORT. To the authors knowledge, this is the first reported cantilever with on-chip actuation that provides a direct measurement of tip-sample interaction force. This development creates the opportunity for high-speed off-resonance imaging and force spectroscopy with miniaturized cantilevers.

In the following, Section 2 introduces a mathematical model of the cantilever deflection and predicts the sensitivity of the actuator and sensor. Section 3 presents a comparison between the mathematical model described and finite element analysis. In Section 4, the cantilever

Table 2
Comparison of common cantilever actuation techniques for AFM.

Technique	Commercial	Sample exceptions	Response time	MEMS compatible	References
Electrothermal	Yes	Temperature sensitive	Slow	Yes	[25–27]
Magnetic driven	Yes	Magnetic sample	Fast	No	[28–31]
Photothermal	Yes	Temperature/light sensitive	Fast	No	[11,32-34]
Piezoelectric	No	–	Fast	Yes	[35–38]

instrumentation is detailed, including the MEMS fabrication process and read-out circuit. Section 5 introduces the experimental setup used to calibrate the system. Section 6 presents the results obtained and discussion. Section 7 presents the conclusions and future work.

2. Mathematical modeling

A mathematical model is presented to aid in the positioning of the sensors and actuator. The tip displacement equations presented offer insights into the required dimensions of the sensors, actuator, and cantilever to obtain a system with specified stiffness and free-air amplitude. Throughout the text, tip force and tip displacement refer to a measurement taken close to the free-end of the cantilever, where a tip is traditionally placed. The detailed derivation of the equations is presented in A.

In cantilevers with integrated sensing and actuation, the sensor is positioned parallel to the actuator. The latter is usually located at the base for maximum tip displacement and maximum strain induced at the sensors. Positioning one sensor far away from the actuator allows it to be most sensitive to tip force, as described in the mathematical model.

2.1. Piezoelectric equations

Consider a homogeneous, isotropic, rectangular cantilever system with a piezoelectric actuator and two sensors, S_1 and S_2, as shown in Fig. 1.

Following the IEEE standard, the piezoelectric materials are modeled as [69].

$$D_3 = d_{31}\sigma_1 + \xi_{13}^{\sigma}E_{F3}, \tag{1}$$

$$\epsilon_1 = S_{13}^{E}\sigma_3 + d_{31}E_{F3}, \tag{2}$$

where (1) is used for sensing and (2) is used for a piezoelectric actuation. The variable D_3 is the electric displacement vector along the z-axis, ξ is the permittivity constant, σ_1 is the applied stress along the x-axis, d_{31} is the strain constant of the sensor, E_{F3} is the applied electric field, ϵ_1 is the strain induced on the x-axis, S_{13}^{E} is the compliance coefficients constant, and σ_3 is the stress applied to the actuator along the z-axis.

Using Eq. (1), the charge on a piezoelectric sensor when no external electrical field applied is [69].

$$q = d_{31}w_sE_s\int_{x_1}^{x_2}\epsilon(z)dx, \tag{3}$$

where E_s is the Young's modulus of the sensor, w_s is the sensor width, and $\epsilon(z)$ is the induced surface strain. The generated charge depends directly on the induced strain on the sensor.

2.2. Charge and tip displacement induced by piezoelectric actuation

The tip displacement u_z along the x-axis induced by a piezoelectric actuator is

$$u_z(x) = \left\{ \begin{array}{ll} \frac{k_\alpha d_{31}}{2t_p}\cdot V_{act}\cdot\frac{w_p}{w_c}\cdot x^2, & \text{for} 0 \le x \le L_p \\ \frac{k_\alpha d_{31}}{2t_p}\cdot V_{act}\cdot\frac{w_p}{w_c}\cdot L_p\cdot(2x - L_p), & \text{for} L_p < x \le L_c \end{array} \right\}. \tag{4}$$

where L_p is the actuator's length and L_c is the cantilever's length.

Evaluating the displacement at $x = L_c$ yields the tip displacement,

$$d_V = \gamma_{act}V_{act}, \tag{5}$$

where the actuator gain γ_{act} is

$$\gamma_{act} = \frac{k_\alpha d_{31}}{2t_p}\frac{w_p}{w_c}L_p(2L_c - L_p), \tag{6}$$

in units of [m/V].

The induced charge on sensors S_1 and S_2 due to the piezoelectric actuation are

$$\left\{ \begin{array}{l} q_{S1,V} = d_{31}^2 w_1 E_s(k_\alpha z + k_\epsilon)\frac{1}{t_p}\frac{w_p}{w_c}(a_2 - a_1)V_{act} \\ q_{S2,V} = 0, \end{array} \right\} \tag{7}$$

where the points a_1 and a_2 are the starting and finishing position of sensor S_1. Note that the charge is zero for a sensor placed outside the area where the actuator is positioned.

2.2.1. Feedthrough in the generated charge

Due to the piezoelectric actuator and small distance between actuator and sensors [70], an electric feedthrough charge is induced on each sensor in response to the voltage applied at the actuator. Electric feedthrough is a well-known phenomenon with piezoelectric actuators for MEMS devices [71]. The parasitic capacitance dominates the signal generated by the piezoelectric sensors given the micro dimensions of the devices, which have sensing capacitance comparable to the parasitic capacitance [64]. When measuring the charge for each sensor generated due to the piezoelectric actuation, the component related to the electric feedthrough is mixed with the generated charge from the actual tip

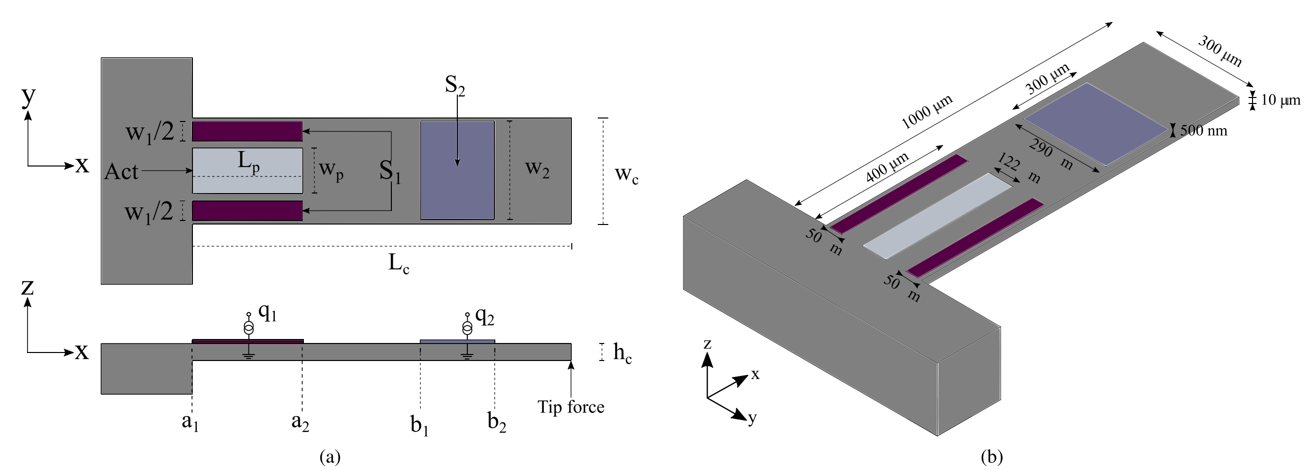

Fig. 1. Cantilever system with dual sensing and integrated actuation. (a) Two-dimensional view highlighting the variables used in the mathematical model. Sensor 1 is parallel to the actuator, at the base, whereas sensor 2 is placed close to the cantilever free-end. (b) Dimensions for the cantilever used for the mathematical model and finite element analysis.

displacement. As such, both parts are not separable unless one knows either the parasitic capacitance or the sensitivity to the tip displacement. However, a precise estimate of the parasitic capacitance can be cumbersome to find.

The approach chosen is to model the feedthrough and include it in the charge model. This charge can be modeled as a capacitor, and the feedthrough charge is obtained by multiplying the feedthrough capacitance by the applied voltage on the piezoelectric actuator [46]. The generated charge in each sensor, then, becomes

$$\left\{\begin{array}{l} q_{S1,V} = \left(d_{31}^2 w_1 E_s (k_\alpha z + k_\epsilon)\dfrac{1}{t_p}\dfrac{w_p}{w_c}(a_2 - a_1)\right)V_{act} \\ \qquad +(c_{1FT})V_{act}, \\ q_{S2,V} = c_{2FT}V_{act}, \end{array}\right\} \tag{8}$$

where c_{1FT} and c_{2FT} are the feedthrough capacitance of each sensor, in units of [C/V].

As the tip displacement is of interest, one can rewrite the generated charge equations to relate to it. Rewriting the charge equation for a piezoelectric actuation in terms of tip displacement by substituting (5) into (8) yields

$$\left\{\begin{array}{l} q_{S1,V} = \left(d_{31}^2 w_1 E_s (k_\alpha z + k_\epsilon)\dfrac{1}{t_p}\dfrac{w_p}{w_c}(a_2 - a_1)\right)\gamma_{act} d_V \\ \qquad +(c_{1FT})\gamma_{act} d_V \\ q_{S2,V} = c_{2FT}k_{act}d_V. \end{array}\right\} \tag{9}$$

2.3. Charge and tip displacement induced by tip force

The tip displacement of a cantilever due to a tip force, (see detailed derivation in A) in terms of the cantilever's stiffness k_c, is

$$d_F = \frac{F_{tip}}{k_{sys}}, \tag{10}$$

and k_c is expressed as,

$$k_c = 3\frac{E_r I_r}{L_c^3}. \tag{11}$$

The induced charge for sensors S_1 and S_2 for a tip force is

$$\left\{\begin{array}{l} q_{S1,F} = -\dfrac{z d_{31} w_1}{2 I_r}\dfrac{E_s}{E_r}\left(-\left(a_2^2 - a_1^2\right) + 2L_c(a_2 - a_1)\right)F_{tip}, \\ q_{S2,F} = -\dfrac{z d_{31} w_2}{2 I_r}\dfrac{E_s}{E_r}\left(-\left(b_2^2 - b_1^2\right) + 2L_c(b_2 - b_1)\right)F_{tip}, \end{array}\right\} \tag{12}$$

where a_1 and a_2, b_1 and b_2 are the starting and finishing position of sensor S_1 and S_2.

Similar to the piezoelectric actuation, it is possible to rewrite the charges based on tip displacement by a tip force as

$$\left\{\begin{array}{l} q_{S1,F} = -\dfrac{z d_{31} w_1}{2 I_r}\dfrac{E_s}{E_r}\left(-\left(a_2^2 - a_1^2\right) + 2L_c(a_2 - a_1)\right)\dfrac{d_F}{k_c} \\ q_{S2,F} = -\dfrac{z d_{31} w_2}{2 I_r}\dfrac{E_s}{E_r}\left(-\left(b_2^2 - b_1^2\right) + 2L_c(b_2 - b_1)\right)\dfrac{d_F}{k_c}. \end{array}\right\} \tag{13}$$

2.4. Simultaneous displacement from tip force and piezoelectric actuation

For a linear system, when the cantilever is under both a tip force and a piezoelectric actuation voltage, the total tip displacement d_T is obtained by adding the displacements as

$$d_T = d_V + d_F. \tag{14}$$

For the charges of the sensors, the total generated charge $q_{S1,T}$ and $q_{S2,T}$ are

$$\left\{\begin{array}{l} q_{S1,T} = q_{S1,V} + q_{S1,F} \\ q_{S2,T} = q_{S2,V} + q_{S2,F}. \end{array}\right\} \tag{15}$$

Expressing the charges in terms of displacements yields

$$\left\{\begin{array}{l} q_{S1,T} = \lambda_1 d_V + \lambda_3 d_F, \\ q_{S2,T} = \lambda_2 d_V + \lambda_4 d_F, \end{array}\right\} \tag{16}$$

where the constants λ_1 to λ_4 are

$$\left\{\begin{array}{l} \lambda_1 = \left(d_{31}^2 w_1 E_s (k_\alpha z + k_\epsilon)\dfrac{1}{t_p}\dfrac{w_p}{w_c}(a_2 - a_1)\right)\gamma_{act} \\ \qquad +(c_{1FT})\gamma_{act}, \\ \lambda_2 = c_{2FT}\gamma_{act}, \\ \lambda_3 = -\dfrac{z d_{31} w_1}{2 I_r}\dfrac{E_s}{E_r}\left(-\left(a_2^2 - a_1^2\right) + 2L_c(a_2 - a_1)\right)\dfrac{1}{k_c}, \\ \lambda_4 = -\dfrac{z d_{31} w_2}{2 I_r}\dfrac{E_s}{E_r}\left(-\left(b_2^2 - b_1^2\right) + 2L_c(b_2 - b_1)\right)\dfrac{1}{k_c}. \end{array}\right\} \tag{17}$$

Eq. (16) can be expressed in a matrix form,

$$\begin{bmatrix} q_{S1,T} \\ q_{S2,T} \end{bmatrix} = \begin{bmatrix} \lambda_1 & \lambda_3 \\ \lambda_2 & \lambda_4 \end{bmatrix} \cdot \begin{bmatrix} d_V \\ d_F \end{bmatrix}, \tag{18}$$

Inverting matrix (18) so that one can recover the displacements yields

$$\begin{bmatrix} d_V \\ d_F \end{bmatrix} = \begin{bmatrix} \psi_1 & \psi_3 \\ \psi_2 & \psi_4 \end{bmatrix} \cdot \begin{bmatrix} q_{S1,T} \\ q_{S2,T} \end{bmatrix} \tag{19}$$

For an AFM, the total tip displacement and tip force are of interest. Using (14) and adding row one with row two and multiplying the second row by the stiffness defined in (A.11) yields

$$\begin{bmatrix} d_T \\ F_{tip} \end{bmatrix} = \begin{bmatrix} \psi_1 + \psi_2 & \psi_3 + \psi_4 \\ \psi_2 \cdot k_c & \psi_4 \cdot k_c \end{bmatrix} \cdot \begin{bmatrix} q_{S1,T} \\ q_{S2,T} \end{bmatrix}, \tag{20}$$

Eq. (20) allows one to recover the tip displacement and tip force simultaneously on a cantilever.

3. Finite element analysis

A finite element analysis (FEA) was carried to validate the mathematical model. The FEA was modeled using ANSYS Workbench and the PiezoAndMEMS extension. The dimensions are shown in Fig. 1 (b) and Table 4. Table 3 shows the material properties used in ANSYS.Table 4.

The input voltage applied is 5 V, and the tip displacement is 1 μ N. Fig. 2 shows the induced surface strain on the cantilever for a tip force and a piezoelectric actuation, respectively. For piezoelectric actuation, the strain is concentrated where the actuator is located. The induced strain where the actuator is not located corresponds to less than 1% of the strain where the piezoelectric actuator is located. The strain is highest at the base for the tip force and linearly reduces along the x-axis to zero at the tip.

Sensor S_2 is placed close to the free-end of the cantilever to be more sensitive to tip force. Although S_2 still generates charge for a piezoelectric voltage applied on the actuator, this charge is only due to the intrinsic electric feedthrough. Table 5 summarizes the FEA for tip displacement and the generated charges of each sensor, induced by

Table 3
Material properties for silicon and aluminum nitride used in ANSYS.

Parameter	Silicon	Aluminum Nitride
Young's modulus [GPa]	169	396
Density [kg/m^{-3}]	2500	3260
Poisson's ratio	0.30	0.30
Strain constant - $d_{31}[m/V]$	–	$2.0 \cdot 10^{-12}$[72–74]
Dielectric constant	–	10.2[75,76]

Table 4
Cantilever's parameters for the mathematical model and FEA.

Parameter	Value [nm]
L_c	1000
w_c	300
t_c	10
L_p	400
w_p	122
t_p	0.5
w_1	100
a_1	0
a_2	400
w_2	290
b_1	600
b_2	900

piezoelectric actuation and tip force, with feedthrough included. Eqs. (8) and (12) were used to calculate the charge and Eq. (5) and (A.11) were used to calculate the tip displacement. For the mathematical model, the parasitic capacitance for sensors S_1 and S_2 were obtained through ANSYS Maxwell.

The absolute difference in charge for sensors 1 and 2 for a piezoelectric actuation is 0.61 fC and 0.33 fC, respectively. For a tip force acting on the cantilever, the difference is 4.22 fC and 4.32 fC.

The tip displacement is 121.7 nm for the mathematical model and 125.5 nm for the FEA model, with a difference of 3.8 nm. The tip displacement resultant of a tip force is 60.04 nm and 60.23 nm for the mathematical and FEA models, respectively. The difference is 0.19 nm between the models. Fig. 3 shows the normalized displacement profile along the x-axis for the cantilever system for a piezoelectric actuation and tip force. The displacements behave differently from each other, shown in Eqs. (A.5) and (A.9). As seen in Fig. 3, the mathematical model describes the displacements in accordance with the FEA.

As described in the mathematical model and validated by the FEA, the strain for a piezoelectric actuator is concentrated at the region where the actuator is placed and insignificant elsewhere. For a tip force, the strain is highest at the base and zero at the free-end. The findings confirm the guidelines used to place the sensors on the cantilever, i.e., one sensor parallel to the actuator and one closer to the free-end. By placing sensor S_2 close to the free-end of the cantilever, one can obtain two independents measurements, since piezoelectric actuator and tip force lead to different bending shapes.

The mathematical model describes the system on one dimension, whereas ANSYS Workbench allows for a three- dimensional analysis. As such, the difference between the values obtained by the two models can be attributed to simplifications on the mathematical model. Layer

Table 5
Tip displacement and generated charge comparison between FEA and analytical models for (a) a piezoelectric actuation and (b) a tip force. The results include feedthrough.

Parameter	AN Model	FEA	Error (%)
(a) Piezoelectric actuation			
Tip displacement [nm]	121.7	125.5	3.12
Charge at Sensor 1 [fC]	51.61	52.12	0.99
Charge at Sensor 2 [fC]	1.98	2.31	16.66
(b) Tip force			
Tip displacement [nm]	60.04	60.23	0.31
Charge at Sensor 1 [fC]	21.27	17.05	19.8
Charge at Sensor 2 [fC]	14.45	10.13	29.9

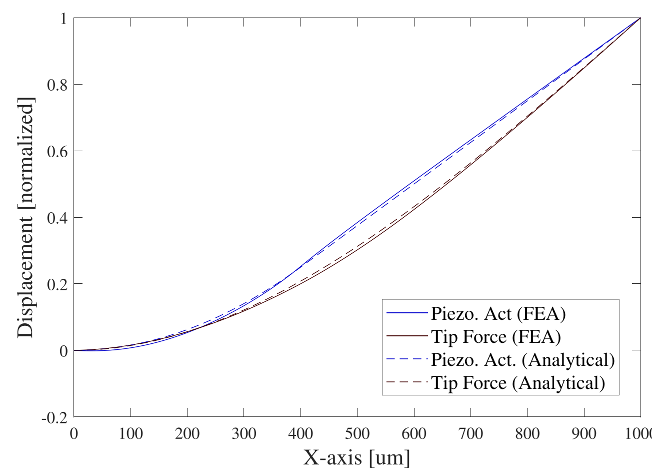

Fig. 3. Cantilever tip displacements due to a tip force and piezoelectric actuation along the cantilever beam obtained from the mathematical model and finite element analysis. The displacement has been normalized to detail the difference in the displacement profiles induced by tip force and piezoelectric actuation.

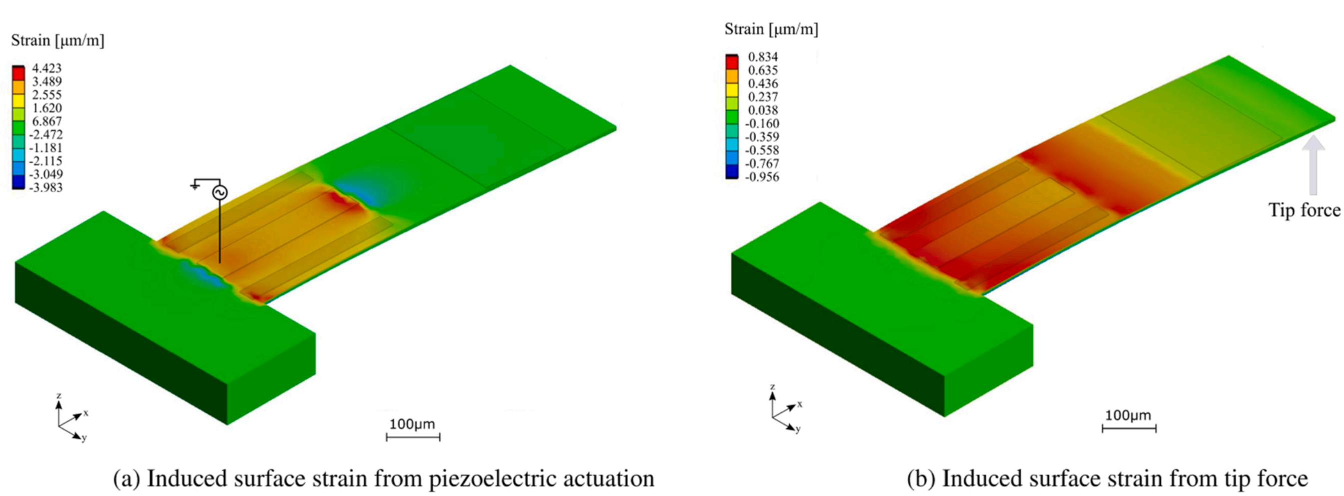

Fig. 2. Strain distribution at the surface of the cantilever for (a) a piezoelectric actuation with $V_{act} = 5V$ and (b) a tip force of $1\mu N$.

modeling and three-dimensional analysis can be integrated within the mathematical model at the cost of simplicity.

4. Cantilever instrumentation

4.1. Cantilever

The cantilever used in this work is shown in Fig. 4. The dimensions of the cantilever and the piezoelectric actuator and sensors are detailed in Fig. 1 (b). The piezoelectric regions are electrically connected to the read-out circuit via the bonding pads at the chip base, as can be seen in Fig. 4 (b). A guard trace is placed around the actuator to mitigate the feedthrough from the piezoelectric actuators to the two sensors [63]. The base of the chip measures 3.7 mm by 1.6 mm.

4.2. MEMS fabrication

The microcantilever chip is fabricated by MEMSCAP using the PiezoMUMPS process. It allows the fabrication of MEMS devices with piezoelectric regions using a 5-mask level Silicon-On-Insulator (SOI) patterning and etching process [77]. In the PiezoMUMPS fabrication process, a 400 μ m SOI wafer is used as the substrate. Mechanical structures, such as suspended cantilevers, are obtained by etching the backside of the substrate layer followed by an oxide etch. The thickness of the silicon after the etch is 10 μ m. A 0.5 μ m thick piezoelectric layer of aluminum nitride is deposited on top of the silicon layer. Subsequently, a 0.2 μ m thick layer of oxide is placed. Finally, a 1 μ m aluminum and 0.2 μ m chrome layer is deposited and used for electrical connections. The layer stack up is shown in Fig. 5 (a).

4.3. Charge amplifier read-out circuit

A charge amplifier circuit topology is used to convert the piezoelectric charge generated from deflections to a voltage level suitable for interfacing with a data acquisition system. The schematic of the readout circuit is shown in Fig. 5 (a). It comprises of three amplification stages. The first stage is a charge to voltage amplifier and the second and third are voltage amplifiers with a passive high pass filter between the first and second stages.

The input of the circuit is the generated charge of the two piezoelectric sensors. The transfer function of the circuit for the first stage is given by [37].

$$H_f(s) = \frac{Y(s)}{U(s)} = -\frac{R_f s}{R_f C_f s + 1}. \tag{21}$$

The charge amplifier acts as a high-pass filter with a cut-off frequency of $\omega_c = \left(R_f C_f\right)^{-1}$. For frequencies where $\omega \gg \omega_c$, the transfer function can be simplified to a static gain and be written as

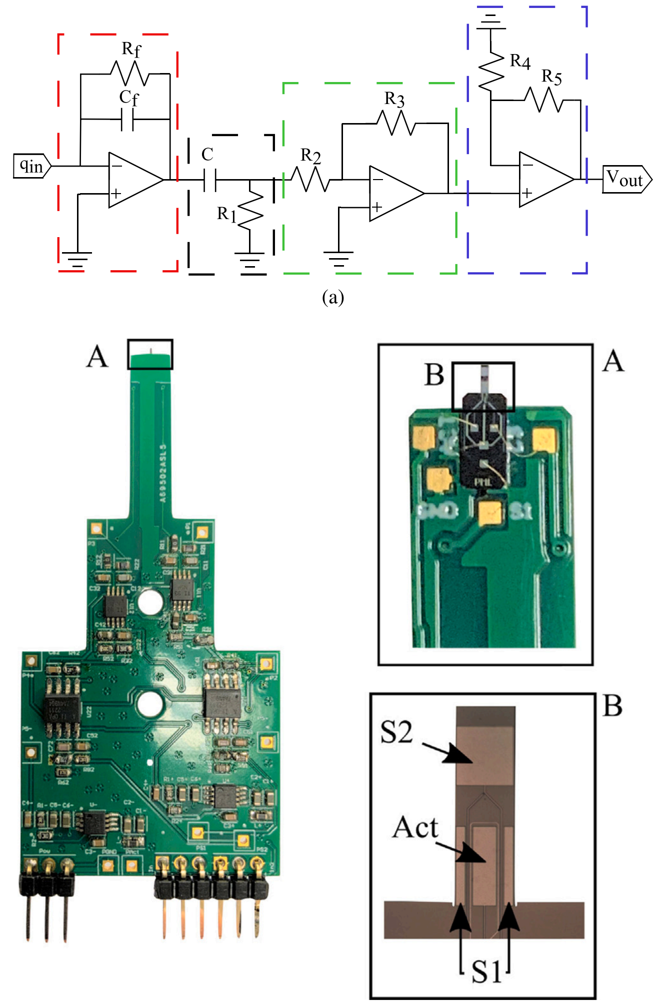

Fig. 5. (a) Charge amplifier circuit showing the first (red), second (green) and third (blue) stages and the passive high-pass filter (black). (b) Photo of the fabricated charge amplifier read-out circuit. Inset A shows the cantilever bonding interface on the backside of the PCB. Inset B shows the manufactured cantilever in detail.

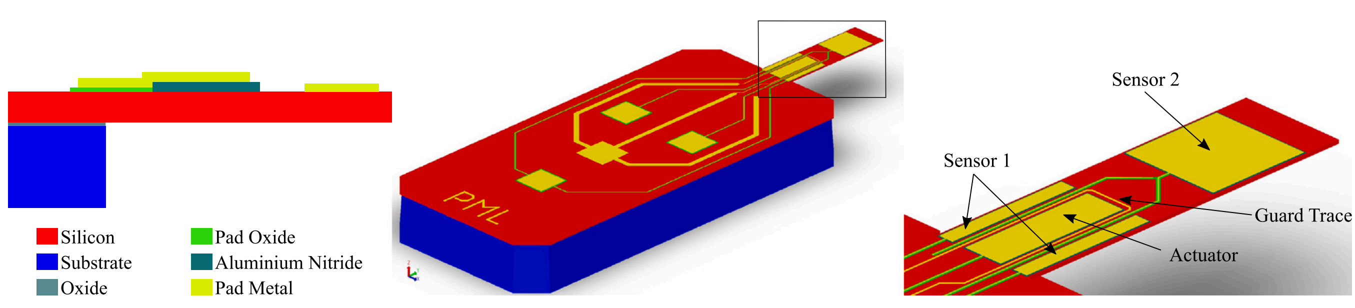

Fig. 4. (a) PiezoMUMPS layer stack fabrication process. (b) Rendering of the microcantilever and chip base where the bonding pads are located. (c) Detail of the cantilever rendering, highlighting the sensors and actuator. A guard trace is placed around the actuator to reduce electric feedthrough.

$$A_1 = -\frac{1}{C_f}. \tag{22}$$

The passive high pass filter can be stated as

$$H_1(s) = \frac{s}{s + \omega_{c1}}, \tag{23}$$

where $\omega_{c1} = (C(R_1//R_2))^{-1}$. Similarly, away from the cut-off frequency of the filter, the transfer function can be simplified to a gain of one.

The second and third stages are voltage amplifiers and their gains can be expressed together as

$$A_{23} = -\frac{R_3}{R_2}\left(1 + \frac{R_5}{R_4}\right). \tag{24}$$

For frequencies $\omega \gg \omega_c$ and $\omega \gg \omega_{c1}$, the total gain of the circuit is given by

$$A_{total} = \left(\frac{1}{C_f}\right)\left(\frac{R_3}{R_2}\right)\left(1 + \frac{R_5}{R_4}\right). \tag{25}$$

The gain of the charge amplifier circuit is in units of [V/C]. The gain of the first stage is $3.03 \cdot 10^{10}$, the gain of the second stage is 5, and the third stage is 24, with a total gain of $3.636 \cdot 10^{12}$ V/C. The cut-off frequency of the first stage is 48 Hz, and the passive high-pass filter is 10 Hz. Fig. 5 (b) shows a photo of the fabricated PCB and interface with the microcantilever. The inset in Fig. 5 (b) shows the wire-bonded chip. The PCB has an ENEPIG (Electroless Nickel Electroless Palladium Immersion Gold) finish to improve the wire-bonding process.

The matrix system in (18) can be rewritten to yield output voltage by multiplying by the total circuit gain of the PCB (25)

$$\begin{bmatrix} V_{S1T} \\ V_{S2T} \end{bmatrix} = \begin{bmatrix} \Lambda_1 & \Lambda_3 \\ \Lambda_2 & \Lambda_4 \end{bmatrix} \cdot \begin{bmatrix} d_V \\ d_F \end{bmatrix}, \tag{26}$$

where the Λ-matrix is equivalent to the λ-matrix multiplied by the total circuit gain A_{total}. The experimental inverse matrix for tip displacement and tip force can now be stated as

$$\begin{bmatrix} d_T \\ F_{tip} \end{bmatrix} = \begin{bmatrix} \Psi_1 + \Psi_2 & \Psi_3 + \Psi_4 \\ \Psi_2 \cdot k_{sys} & \Psi_4 \cdot k_{sys} \end{bmatrix} \cdot \begin{bmatrix} V_{S1T} \\ V_{S2T} \end{bmatrix}, \tag{27}$$

where the Ψ-matrix is the inverse of the Λ-matrix and k_{sys} is the experimentally obtained cantilever spring constant from Section 5.4. In the following section, the matrices from (26) and (27) will be used for th experimental calibration.

5. System calibration

5.1. Experimental setup

The experimental setup to calibrate the integrated force and displacement sensors of the active cantilever is shown in the schematic in Fig. 6 (a), and a photo of the setup is shown in Fig. 6 (b). The active cantilever is mounted on it's read-out circuit and a coarse positioning stage with an opening in the middle. The opening allows a Polytec Scanning Vibrometer (PSV-500) to be focused on the active cantilever to provide an accurate displacement reference measurement. A Tap190Al-G reference cantilever inside a Nanosurf (EasyScan 2) AFM is mounted on top of the active cantilever. The Nanosurf cantilever is aligned so that its tip touches the top of the free end of the active cantilever when landed.

5.2. Piezoelectric actuator calibration

The piezoelectric actuator was calibrated by driving it with a 200 mV chirp signal with the Nanosurf cantilever retracted and recording the displacement using the PSV-500. Fig. 7 shows the frequency response

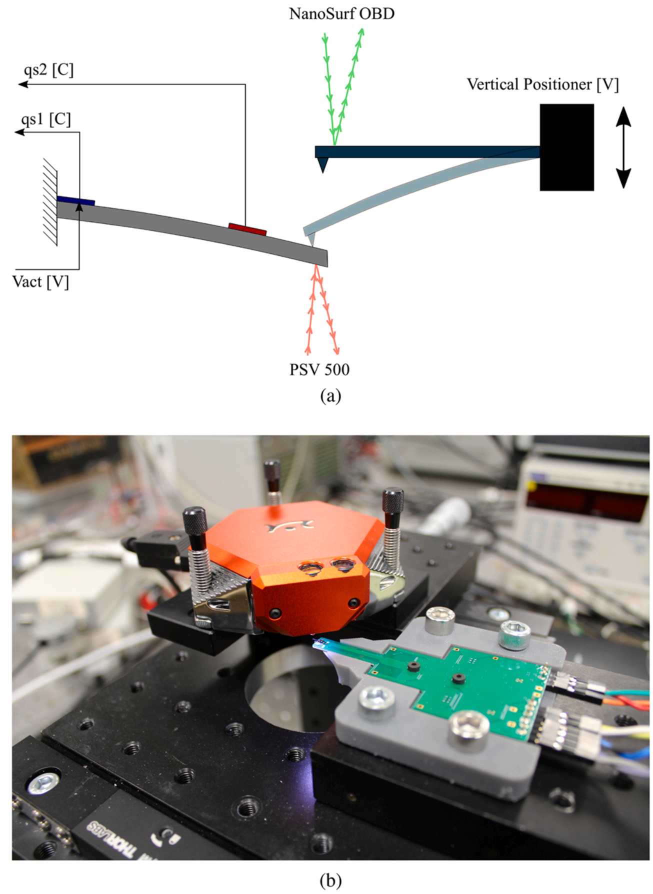

Fig. 6. (a) Schematic for the experimental setup. (b) Experimental setup showing the Nanosurf AFM landed on the active cantilever mounted on the read-out circuit.

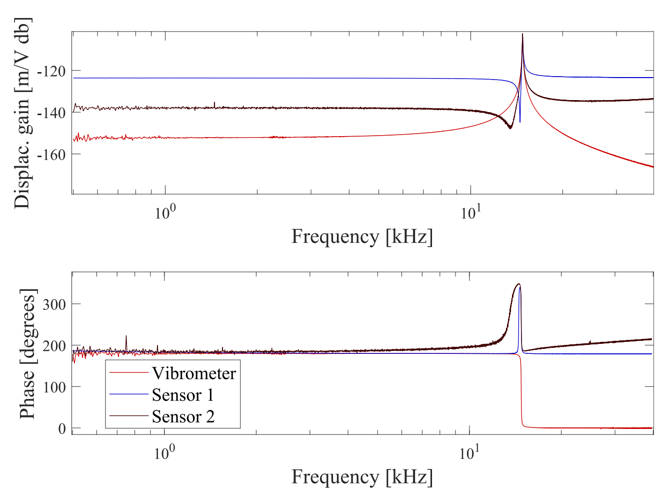

Fig. 7. Frequency responses of the active cantilever measured with the PSV 500 Vibrometer and the integrated sensors.

from integrated actuation to tip displacement and as measured with the integrated sensors. The cantilever actuation gain at the intended frequency of operation of 500 Hz can be found by evaluating the frequency response at that frequency and is given in Table 6.

5.3. Piezoelectric sensor calibration

The measurements with the integrated sensors exhibit electrical

Table 6
Summary of the calibrated sensor parameters for displacement from a piezoelectric actuator.

Parameter	Units	Value
Actuation frequency	Hz	500
Piezoelectric actuator	V	5
Tip displacement	m	$-1.22 \cdot 10^{-7}$
Sensor 1	V	4.64
Sensor 2	V	0.18
γ_{act}	m/V	$-2.44 \cdot 10^{-8}$
Λ_1	V/m	$-3.83 \cdot 10^{7}$
Λ_2	V/m	$-0.15 \cdot 10^{7}$

feedthrough originating from parasitic capacitances between the actuator and sensors. As a result, the frequency response contains an extra complex zero pair near the resonance and the low frequency range shows a significant higher gain due to the additional feedthrough component. As can be seen from Fig. 7, the feedthrough from the actuator to sensor S_1 is higher than to sensor S_2. This is due to sensor S_2 having a higher sensing capacitance and being located further away from the actuator. With the assumption that the electrical feedthrough is minimized at the resonance frequency, the piezoelectric sensors are calibrated for displacement by aligning the magnitude of the frequency responses of each sensor and the tip displacement. The sensor sensitivities at the intended frequency of operation of 500 Hz can be found by evaluating the frequency response at that frequency and are given in table 3. Since the sensitivities contain the feedthrough component, its effect is mitigated when the model is inverted. Note, the static model (Eqs. (5) and (8)) is only valid for frequencies sufficiently lower than the resonant frequency. The calibration constants (Λ_1 and Λ_2) are obtained by dividing the voltage of each sensor by the tip displacement and are stated in Table 6.

5.4. Stiffness calibration

The stiffness of each cantilever is needed to calibrate the system for a displacement induced by a tip force. The calibration of AFM cantilevers is usually performed using the thermal noise method [78]. The thermal method uses the vibrations caused in the cantilever due to the Brownian motion. When the thermal noise method is implemented using Laser Doppler Vibrometry [20], the stiffness of the cantilever is given by

$$k = (2\pi f)^2 \frac{k_B T}{\overline{v}^2}, \tag{28}$$

where f is the first resonance frequency, k_B is the Boltzmann constant, T is the equilibrium temperature, and $\overline{v}$ is the mean velocity obtained from a Lorentzian fit to the velocity power spectrum.

The velocity of the thermal noise motion was measured with a vibrometer (Micro System Analyzer vibrometer - Polytec MSA-100–3D) in the time domain. Fig. 8 shows the thermal noise of the Nanosurf cantilever and the active cantilever around their respective first resonance frequencies. The spectra are obtained from the power spectrum density estimates using Welch's method with 64 averages, no overlap, and Hanning window. The measured stiffness of the Nanosurf cantilever is 54.63 N/m, and the active cantilever is 13.71 N/m.

5.5. Tip force calibration

For the tip force calibration, the Nanosurf cantilever was landed on the active cantilever, and the piezoelectric actuator was grounded. The Nanosurf cantilever was landed using a setpoint of 50 nN. After the landing procedure is completed, the z-axis controller output was frozen such that it maintains its current output. With both cantilevers in contact, the vertical positioner was excited with a 250 mV signal at 500 Hz. The resulting movement of the connected cantilever system was measured with the piezoelectric sensors, with the OBD and with the vibrometer. The constants from each sensor (Λ_3 and Λ_4) are obtained by

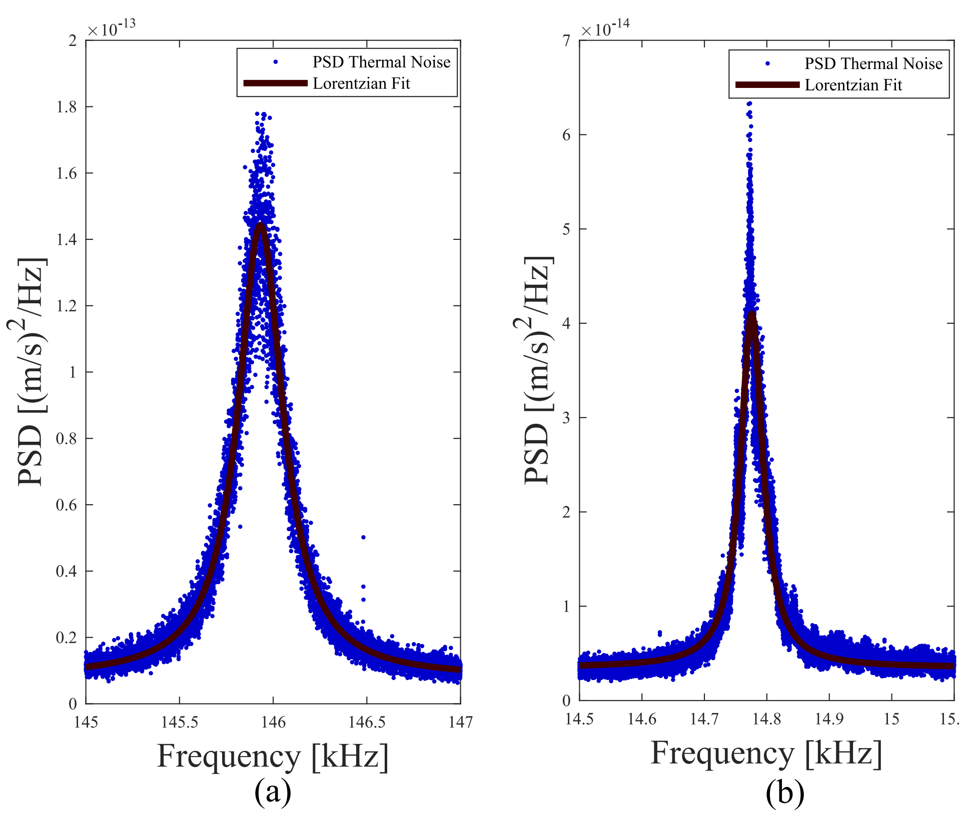

Fig. 8. Thermal noise measurement of (a) Nanosurf cantilever and (b) active cantilever.

Table 7
Summary of the calibrated sensor parameters for displacement from a tip force.

Parameter	Units	Value
Actuation frequency	Hz	500
Vertical positioner	V	0.250
Tip displacement	m	$3.56 \cdot 10^{-8}$
Sensor 1	V	0.048
Sensor 2	V	0.016
OBD	V	− 0.05
Λ_3	V/m	$0.134 \cdot 10^{7}$
Λ_4	V/m	$0.046 \cdot 10^{7}$
c_{OBD}	m/V	$-6.61 \cdot 10^{-7}$

dividing the voltage of each sensor by the tip displacement obtained from the vibrometer measurements. c_{OBD} is the constant used to calibrate the OBD signal to displacement and, using its stiffness from Section 5.4, to tip force. The experimentally obtained parameters are stated in Table 7.

5.6. Experimental calibration matrix

From the experiments described in Sections 5 and 5.4 (Tables 6 and 7), the calibration matrix of the system is

$$[\Lambda] = \begin{bmatrix} \Lambda_1 & \Lambda_2 \\ \Lambda_3 & \Lambda_4 \end{bmatrix} = \begin{bmatrix} -3.83 \cdot 10^{7} & 1.34 \cdot 10^{6} \\ -1.48 \cdot 10^{6} & 4.59 \cdot 10^{5} \end{bmatrix}. \tag{29}$$

Inverting the Λ-matrix yields the experimental Ψ-matrix

$$[\Psi] = \begin{bmatrix} \Psi_1 & \Psi_2 \\ \Psi_3 & \Psi_4 \end{bmatrix} = \begin{bmatrix} -2.944 \cdot 10^{-8} & 8.606 \cdot 10^{-8} \\ -9.491 \cdot 10^{-8} & 2.457 \cdot 10^{-6} \end{bmatrix}. \tag{30}$$

Using the transformation from (27) and the stiffness found in Section 5.4, the experimental matrix for tip force and tip displacement becomes

$$\begin{bmatrix} d_T \\ F_{tip} \end{bmatrix} = \begin{bmatrix} -1.243 \cdot 10^{-7} & 2.543 \cdot 10^{-6} \\ -5.505 \cdot 10^{-6} & 1.425 \cdot 10^{-4} \end{bmatrix} \cdot \begin{bmatrix} V_{S1T} \\ V_{S2T} \end{bmatrix}. \tag{31}$$

Eq. 31 is used to recover the tip displacement and tip force using the measured voltages of sensors S_1 and S_2. The stiffness of the system k_{sys} is the sum of the stiffness of both cantilevers obtained through the thermal noise method.

6. Simultaneous tip displacement and tip force measurement

After calibration, the active cantilever is used for simultaneous force and displacement sensing. First, the Nanosurf cantilever was landed on top of the active cantilever using a setpoint of 50 nN. After the landing procedure is completed, the z-axis controller output was frozen such that it maintains its current output. After landing is complete, the nanosurf cantilever was retracted slightly using the stepper motor and the active cantilever was excited by a sinusoidal waveform of 500 Hz and amplitude of 5 V, which translates to a free-air amplitude of 122 nm. Retracting the cantilever allows the active cantilever to approach, engage and retract from the Nanosurf cantilever which simulates an off-resonance tapping-mode AFM operation.

The tip displacement, voltage of the piezoelectric sensors and OBD system were measured with a sample frequency of 250 kHz, and post-processed offline using MATLAB. The post-processing steps in MATLAB include the integration of the displacement since the vibrometer naturally captures velocity information in the time-domain. Additionally, the signals of each sensor were filtered to eliminate a small noise component at 50 Hz originating from electric grid noise. The results shown in Fig. 9 were obtained multiplying the voltage of each sensor in the time-domain by the matrix in Eq. (31).

The results comparing the displacement obtained from the vibrometer and the integrated sensor are shown in Fig. 9 (a). The measurement curves are characterized by two distinctive regimes: during the contact phase the two cantilevers move simultaneously and follow the

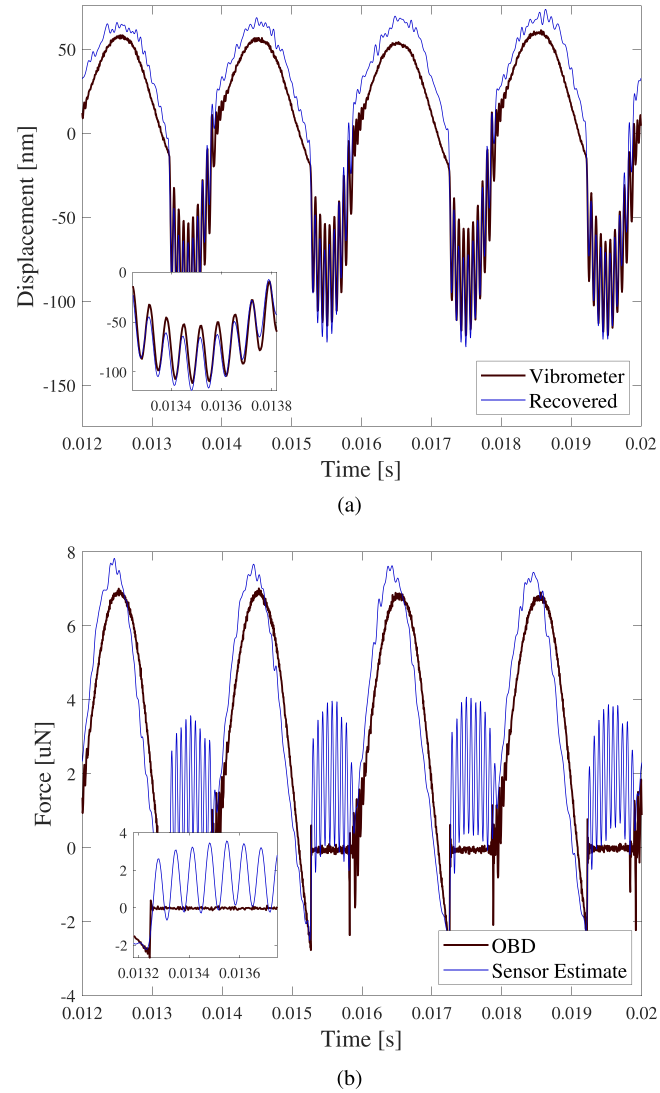

Fig. 9. Simultaneous displacement and force sensing with the active cantilever. (a) shows the tip displacement compared with the vibrometer and (b) presents the tip force compared with the OBD system. Both insets in (a) and (b) show the ringing effect after the snap-off between the cantilevers.

sinusoidal excitation. When the contact is broken, the active cantilever shows transient oscillations at the resonance frequency of 14.88 kHz. It can be seen that the integrated sensor output follows the reference measurement from the vibrometer accurately. When the contact is broken, the transient oscillations at the resonance frequency are superimposed on the sinusoidal motion of the active cantilever. Once the two cantilevers are in contact, the ringing dies down quickly. This is

Table 8
Sensitivity to displacement of each sensor and actuator gain for (a) a piezoelectric actuation and (b) a tip force.

Parameter	AN Model	FEA	Experimental
(a) Piezoelectric actuation			
Actuator gain [nm/V]	24.34	25.1	24.4
S_1 [fC/nm]	0.42	0.415	10.53
S_2 [fC/nm]	0.016	0.018	0.412
(b) Tip force			
S_1 [fC/nm]	0.354	0.283	0.368
S_2 [fC/nm]	0.16	0.240	0.126

expected, as the system mechanic properties change once in contact, acquiring a different combined Q-factor, stiffness, and resonance frequency, all of which determine the transient response.

During the measurement, the OBD sensor is used as a reference measurement for tip force which is plotted in Fig. 9 (b) and compared with the recovered force by the sensors. The tip force follows a sinusoidal shape, originating from the excitation of the piezoelectric actuator. After contact is lost, the active cantilever shows transient oscillations at the resonance frequency. The inset details the snap-off moment between the cantilevers. Table 8 presents a comparison between the analytical model, FEA and the experimental results obtained. The experimental sensitivities were obtained by dividing the Λ values by the gain of read-out circuit and the analytical and FEA sensitivities are based from the results shown in Table 5. Sensor S_1 generates charge from the induced strain from the actuator and the electric feedthrough, whereas sensor S_2 is only affected by electric feedthrough. However, sensor S_2 displays a sensitivity to tip force 3.27 times lower than to piezoelectric actuation. In reducing the feedthrough, the sensitivity of sensor S_2 can be further improved to detect tip force only. Note that sensor S_2 is placed very close to the free-end, where the strain is almost zero.

The actuator gain for the analytical model, FEA and the experimental results are similar. The higher sensitivity displayed by the sensors experimentally for a piezoelectric actuation is due to the higher experimental feedthrough.

For a tip force, the experimental sensitivity is similar for sensor S_1. Sensor S_2 displays a lower sensitivity and that is explained by the point of application of force. Experimentally, the force applied is not at the tip, rather it is close to it. As the strain along the cantilever reduces to zero where the force is applied, a reduction on the strain for sensor S_2 affects it more proportionally than sensor S_1.

7. Conclusions

The article describes a new cantilever system with on-chip actuation and dual sensors capable of independently measuring the tip displacement and tip force acting on the cantilever. The approach reduces problems with on-chip actuation and sensing where the measured deflection includes contributions from both the tip force and actuation signal. In this work, piezoelectric layers are used for both the actuators and sensors which does not allow detection of static deflections, which is required for contact modes. However, these sensors are ideal for off-resonance tapping mode, which is the focus of this work.

Despite the large reduction in mechanical cross-coupling between the actuator and force sensor, electrical cross-coupling was still observed to be significant. This required the use of a calibration process to identify the electrical cross-coupling terms and cancel them during operation.

To validate the proposed cantilever, a test system was constructed that uses a second AFM to apply a known force, while an interferometer is used to directly measure the true displacement. Experimental results show a close correlation between the force and displacement measured by the on-chip sensors, and the external reference sensors. The most significant disagreement was due to oscillation of the integrated cantilever that is induced at the moment of detachment during force spectroscopy.

Future work aims to reduce issues with oscillation during detachment by actively reducing the Q-factor. This is expected to significantly reduce oscillation while the cantilever is detached from the sample and will increase the rate of force spectroscopy. AFM tips will also be added to the cantilevers using a standard MEMs post-processing method, which will enable imaging experiments using an off-resonance tapping mode, or force spectroscopy.

CRediT authorship contribution statement

Natã Franco Soares de Bem: Conceptualization, Methodology, Software, Validation, Formal analysis, Investigation, Writing – original draft, Visualization, Project administration. **Michael Ruppert**: Supervision, Investigation, Writing – review & editing. **Yuen Yong**: Funding acquisition, Supervision, Writing – review & editing. **Andrew Fleming**: Supervision, Investigation, Writing – review & editing.

Declaration of Competing Interest

The authors declare that they have no known competing financial interests or personal relationships that could have appeared to influence the work reported in this paper.

Acknowledgements

This work was supported by the Australian Research Council Discovery Project DP170101813.

Appendix A. Mathematical model

A.1. Piezoelectric equations

Eq. (2) is used to model the piezoelectric actuator [69]. When no external stress is applied, the surface strain induced by a voltage V_{act} applied to a piezoelectric actuator is given by [15,69].

$$\epsilon = k_\alpha z \frac{w_p}{w_c} \cdot \frac{d_{31} V_{act}}{t_p}, \tag{A.1}$$

where z is the position along the z-axis, t_p is the actuator thickness, w_c is the cantilever width, w_p is the actuator width, and k_α is a constant that is related to the thickness and Young's modulus of the cantilever and defined as [69].

$$k_\alpha = \frac{6E_c E_p t_c t_p (t_c + t_p)}{E_c^2 t_c^4 + E_c E_p (4t_c^3 t_p + 6t_c^2 t_p^2 + 4t_c t_p^3) + E_p^2 t_p^4}, \tag{A.2}$$

with E_c and E_p being the Young's modulus of the cantilever and actuator, respectively, and t_c and t_p are the cantilever's thickness and the actuator's thickness, respectively.

A.2. Charge and tip displacement induced by piezoelectric actuation

Euler-Bernoulli equations are used to model the tip displacement of the cantilever. It can be written as

$$\left[E_r I_r \frac{d^2 u_z}{dx^2}\right] = F_z(x), \tag{A.3}$$

where E_r and I_r are the Young's modulus and second moment of area of the system, respectively and $F_z(x)$ is the applied force along the x-axis in the z-direction.

To solve (A.3), the following boundary conditions are applied. The displacement and slope at the base and the shear force at the tip are zero. The moment

$$M = -E_r I_r \frac{\epsilon}{z}, \tag{A.4}$$

is constant where the actuator is located ($0 \le x \le L_p$) and zero elsewhere ($L_p < x \le L_c$). The induced strain is given by Eq. (A.1).

Solving Eq. A.3 using the above boundary conditions and Eq. (A.1) leads to the displacement u_z along the x-axis,

$$u_z(x) = \left\{ \begin{array}{ll} \frac{k_\alpha d_{31}}{2t_p} \cdot V_{act} \cdot \frac{w_p}{w_c} \cdot x^2, & \text{for} 0 \le x \le L_p \\ \frac{k_\alpha d_{31}}{2t_p} \cdot V_{act} \cdot \frac{w_p}{w_c} \cdot L_p \cdot (2x - L_p), & \text{for} L_p < x \le L_c \end{array} \right\}. \tag{A.5}$$

where L_p is the actuator's length and L_c is the cantilever's length.

The strain can be related to the displacement as

$$\epsilon = \frac{d^2 u_z(x)}{dx^2}. \tag{A.6}$$

From Eq. (A.6) and (A.5), the strain is [15],

$$\epsilon(z) = \left\{ \begin{array}{ll} (k_\alpha z) \frac{d_{31} V_{act}}{t_p} \left(\frac{w_p}{w_c}\right), & \text{for} 0 \le x \le L_p \\ 0, & \text{for} L_p < x \le L_c \end{array} \right\}, \tag{A.7}$$

where L_p is the actuator's length.

Substituting (A.7) into (3), the charge can be expressed as [15].

$$q = \left\{ \begin{array}{ll} d_{31}^2 w_s E_s (k_\alpha z) \frac{1}{t_p} \frac{w_p}{w_c} V_{act}(x)|_{x_1}^{x_2}, & \text{for} 0 \le x \le L_p \\ 0, & \text{for} L_p < x \le L_c \end{array} \right\}, \tag{A.8}$$

where the points a_1 and a_2 are the starting and finishing position of sensor S_1. Note that the charge is zero for a sensor placed outside the area where the actuator is positioned.

A.3. Charge and tip displacement induced by tip force

The cantilever displacement due to tip force is derived following similar procedure. By using Euler-Bernoulli equations in (A.3) with boundaries conditions where the displacement and slope at the base are zero, the shear force at the tip is the force applied and the moment at the tip is zero, the displacement along the x-axis is,

$$u_z(x) = \frac{1}{6E_r I_r}\left(-x^3 + 3L_c x^2\right) F_{tip}, \text{for} 0 \le x \le L_c, \tag{A.9}$$

where, F_{tip} is the applied tip force in the z-axis.

The tip displacement d_F due to a tip force can be evaluated at $x = L_c$ and, from (A.9), yields

$$d_F = \frac{L_c^3 F_{tip}}{3E_r I_r}, \tag{A.10}$$

Expressing Eq. (A.10) in terms of the cantilever's stiffness k_c, yields

$$d_F = \frac{F_{tip}}{k_{sys}}, \tag{A.11}$$

and k_c is expressed as,

$$k_c = 3\frac{E_r I_r}{L_c^3}. \tag{A.12}$$

The strain can be obtained by taking the second derivative of the displacement in (A.9). The surface strain on the cantilever displays a first-order behavior along the x-axis, expressed as,

$$\epsilon(x) = \frac{F_{tip}}{E_r I_r}(-x + L_c), \text{for} 0 \leq x \leq L. \tag{A.13}$$

By substituting (A.13) into (3), the general equation for surface charge induced by tip force is [15].

$$q = -\frac{z d_{31} b_s}{2 I_r} \frac{E_s}{E_r} F_{tip}(-x^2 + 2 L_c x)|_{x_1}^{x_2}. \tag{A.14}$$

where x_1 and x_2 are the starting and finishing positions of the sensor.

References

[1] G. Binnig, C.F. Quate, C. Gerber, Atomic force microscope, Phys. Rev. Lett. 56 (1986) 930–933, https://doi.org/10.1103/PhysRevLett.56.930. ⟨https://link.aps.org/doi/10.1103/PhysRevLett.56.930⟩.

[2] D. Ebeling, B. Eslami, S.D.J. Solares, Visualizing the subsurface of soft matter: Simultaneous topographical imaging, depth modulation, and compositional mapping with triple frequency atomic force microscopy, ACS Nano 7 (11) (2013) 10387–10396, https://doi.org/10.1021/nn404845q, pMID: 24131492. arXiv, ⟨https://doi.org/10.1021/nn404845q⟩.

[3] K.-H. Chung, Wear characteristics of atomic force microscopy tips: A review, Int. J. Precis. Eng. Manuf. 15 (10) (2014) 2219–2230, https://doi.org/10.1007/s12541-014-0584-6.

[4] K. Hayashi, M. Iwata, Stiffness of cancer cells measured with an afm indentation method 49 105–111.10.1016/j.jmbbm.2015.04.030.⟨https://www.sciencedirect.com/science/article/pii/S1751616115001587⟩.

[5] M. Dukic, J.D. Adams, G. Fantner, Piezoresistive afm cantilevers surpassing standard optical beam deflection in low noise topography imaging, Sci. Rep. 5 (2015) 16393.

[6] R. Garcia, R. Perez, Dynamic atomic force microscopy methods, Surf. Sci. Rep. 47 (6) (2002) 197–301, https://doi.org/10.1016/S0167-5729(02)00077-8. ⟨http://www.sciencedirect.com/science/article/pii/S0167572902000778⟩.

[7] C. Godon, J.-M. Teulon, M. Odorico, C. Basset, M. Meillan, L. Vellutini, S. wen W. Chen, J.-L. Pellequer, Conditions to minimize soft single biomolecule deformation when imaging with atomic force microscopy, J. Struct. Biol. 197 (3) (2017) 322–329, https://doi.org/10.1016/j.jsb.2016.12.011. ⟨http://www.sciencedirect.com/science/article/pii/S1047847716302660⟩.

[8] M. Balantekin, F. Değertekin, Optimizing the driving scheme of a self-actuated atomic force microscope probe for high-speed applications, Ultramicroscopy 111 (8) (2011) 1388–1394, https://doi.org/10.1016/j.ultramic.2011.05.006. ⟨http://www.sciencedirect.com/science/article/pii/S0304399111001653⟩.

[9] O. Sahin, S. Magonov, C. su, C.F. Quate, O. Solgaard, An atomic force microscope tip designed to measure time-varying nanomechanical forces, Nat. Nanotechnol. 2 (2007) 507–514, https://doi.org/10.1038/nnano.2007.226.

[10] W. Walczyk, P.M. Schön, H. Schönherr, The effect of PeakForce tapping mode AFM imaging on the apparent shape of surface nanobubbles, J. Phys.: Condens. Matter 25 (18) (2013), 184005, https://doi.org/10.1088/0953-8984/25/18/184005.

[11] A.P. Nievergelt, C. Brillard, H.A. Eskandarian, J.D. McKinney, G.E. Fantner, Photothermal off-resonance tapping for rapid and gentle atomic force imaging of live cells, Int. J. Mol. Sci. 19 (10) (2018), https://doi.org/10.3390/ijms19102984.

[12] H. Schillers, I. Medalsy, S. Hu, A.L. Slade, J.E. Shaw, Peakforce tapping resolves individual microvilli on living cells, J. Mol. Recognit. 29 (2) (2016) 95–101, https://doi.org/10.1002/jmr.2510 (arXiv), ⟨https://onlinelibrary.wiley.com/doi/pdf/10.1002/jmr.2510⟩.

[13] K. Xu, W. Sun, Y. Shao, F. Wei, X. Zhang, W. Wang, P. Li, Recent development of peakforce tapping mode atomic force microscopy and its applications on nanoscience, Nanotechnol. Rev. 7 (2018) 09, https://doi.org/10.1515/ntrev-2018-0086.

[14] A. Nievergelt, N. Banterle, S.H. Andany, P. Gönczy, G. Fantner, High-speed photothermal off-resonance atomic force microscopy reveals assembly routes of centriolar scaffold protein sas-6, Nat. Nanotechnol. 13 (2018) 08, https://doi.org/10.1038/s41565-018-0149-4.

[15] N.F.S. d. Bem, M.G. Ruppert, Y.K. Yong, A.J. Fleming, Integrated force and displacement sensing in active microcantilevers for off-resonance tapping mode atomic force microscopy, Int. Conf. Manip. (2020) 1–6, https://doi.org/10.1109/MARSS49294.2020.9307881.

[16] D. Kirmizis, S. Logothetidis, Atomic force microscopy probing in the measurement of cell mechanics 5 137–45.10.2147/IJN.S5787.

[17] S. IanMoore, Y.K. Yong, Design and characterisation of cantilevers for multi-frequency atomic force microscopy, Micro, Nano Lett. 12 (5) (2017) 315–320.

[18] S.P. Wadikhaye, Y.K. Yong, B. Bhikkaji, S.O. R. Moheimani, Control of a piezoelectrically actuated high-speed serial-kinematic AFM nanopositioner 23 (2) 025030.10.1088/0964–1726/23/2/025030.

[19] N. Gavara, A beginner's guide to atomic force microscopy probing for cell mechanics, Microsc. Res. Tech. 80 (2016) 09, https://doi.org/10.1002/jemt.22776.

[20] M.G. Ruppert, N.F. S.D. Bem, A.J. Fleming, Y.K. Yong, Characterization of active microcantilevers using laser doppler vibrometry, in: S. Oberst, B. Halkon, J. Ji, T. Brown, (Eds.), Vibration Engineering for a Sustainable Future, Springer International Publishing, 355–361.

[21] W. Liu, K. Bonin, M. Guthold, Easy and direct method for calibrating atomic force microscopy lateral force measurements 78 (6). 10.1063/1.2745733.

[22] F. Eghiaian, F. Rico, A. Colom, I. Casuso, S. Scheuring, High-speed atomic force microscopy: Imaging and force spectroscopy, FEBS Lett. 588 (19) (2014) 3631–3638, https://doi.org/10.1016/j.febslet.2014.06.028 (sI: Single molecule techniques - Applications in biology), ⟨http://www.sciencedirect.com/science/article/pii/S001457931400489X⟩.

[23] M. Zawierta, R.D. Jeffery, G. Putrino, K.D. Silva, A. Keating, M. Martyniuk, L. Faraone, Atomic force microscopy with integrated on-chip interferometric readout, Ultramicroscopy 205 (2019) 75–83, https://doi.org/10.1016/j.ultramic.2019.05.011. ⟨http://www.sciencedirect.com/science/article/pii/S0304399118301803⟩.

[24] Nanosurf, Operating Instructions: easyScan 2 STM, Nanosurf AG, 1st Edition. ⟨http://mnil.kaist.ac.kr/mnil1/wp-content/uploads/2019/07/STMManual.pdf⟩.

[25] T. Ivanov, T. Gotszalk, P. Grabiec, E. Tomerov, I. Rangelow, Thermally driven micromechanical beam with piezoresistive deflection readout 67–68 550–556.10.1016/s0167–9317(03)00113–8.

[26] J. Lee, W.P. King, Microcantilever actuation via periodic internal heating 78 (12) 126102.10.1063/1.2818805.

[27] R. Boubekri, E. Cambril, L. Couraud, L. Bernardi, A. Madouri, M. Portail, T. Chassagne, C. Moisson, M. Zielinski, S. Jiao, J.-F. Michaud, D. Alquier, J. Bouloc, L. Nony, F. Bocquet, C. Loppacher, D. Martrou, S. Gauthier, Electrothermally driven high-frequency piezoresistive SiC cantilevers for dynamic atomic force microscopy 116 (5) 054304.10.1063/1.4891833.

[28] B. Lee, C.B. Prater, W.P. King, Lorentz force actuation of a heated atomic force microscope cantilever 23 (5) 055709.10.1088/0957–4484/23/5/055709.

[29] K. Hirata, T. Igarashi, K. Suzuki, K. Miyazawa, T. Fukuma, Wideband magnetic excitation system for atomic force microscopy cantilevers with megahertz-order resonance frequency 10 (1). 10.1038/s41598–020-65980–4.

[30] S. Jarvis, M. Lantz, U. Dürig, H. Tokumoto, Off resonance ac mode force spectroscopy and imaging with an atomic force microscope, Appl. Surf. Sci. 140 (3) (1999) 309–313, https://doi.org/10.1016/S0169-4332(98)00546-7. ⟨http://www.sciencedirect.com/science/article/pii/S0169433298005467⟩.

[31] X. Meng, H. Zhang, J. Song, X. Fan, L. Sun, H. Xie, Broad modulus range nanomechanical mapping by magnetic-drive soft probes 8 (1). 10.1038/s41467–017-02032-y.

[32] H. Yamashita, N. Kodera, A. Miyagi, T. Uchihashi, D. Yamamoto, T. Ando, Tip-sample distance control using photothermal actuation of a small cantilever for high-speed atomic force microscopy, Rev. Sci. Instrum. 78 (8) (2007), 083702, https://doi.org/10.1063/1.2766825 (arXiv), ⟨https://doi.org/10.1063/1.2766825⟩.

[33] R. Wagner, J.P. Killgore, Photothermally excited force modulation microscopy for broadband nanomechanical property measurements 107 (20) 203111.10.1063/1.4935982.

[34] N. Umeda, Scanning attractive force microscope using photothermal vibration 9 (2)1318.10.1116/1.585187.

[35] S.C. Minne, S.R. Manalis, C.F. Quate, Parallel atomic force microscopy using cantilevers with integrated piezoresistive sensors and integrated piezoelectric actuators, Appl. Phys. Lett. 67 (26) (1995) 3918–3920, https://doi.org/10.1063/1.115317 (arXiv), ⟨https://doi.org/10.1063/1.115317⟩.

[36] S.R. Manalis, S.C. Minne, C.F. Quate, Atomic force microscopy for high speed imaging using cantilevers with an integrated actuator and sensor, Appl. Phys. Lett. 68 (6) (1996) 871–873, https://doi.org/10.1063/1.116528 (arXiv), ⟨https://doi.org/10.1063/1.116528⟩.

[37] M.G. Ruppert, S.I. Moore, M. Zawierta, A.J. Fleming, G. Putrino, Y.K. Yong, Multimodal atomic force microscopy with optimized higher eigenmode sensitivity using on-chip piezoelectric actuation and sensing, Nanotechnology 30 (8) (2019), 085503, https://doi.org/10.1088/1361-6528/aae40b.

[38] X. Gao, J. Yang, J. Wu, X. Xin, Z. Li, X. Yuan, X. Shen, S. Dong, Piezoelectric actuators and motors: Materials, designs, and applications 5 (1) 1900716.10.1002/admt.201900716.

[39] P. Huang, S. Andersson, High speed atomic force microscopy enabled by a sample profile estimator 102 (21). 10.1063/1.4808211.

[40] Y.K. Yong, A.J. Fleming, High-speed vertical positioning stage with integrated dual-sensor arrangement 248 184–192.10.1016/j.sna.2016.06.042.

[41] A.J. Fleming, Dual-stage vertical feedback for high-speed scanning probe microscopy 19 (1)156–165.10.1109/tcst.2010.2040282.

[42] P. Huang, S.B. Andersson, Fast scanning in afm using non-raster sampling and time-optimal trajectories, IEEE 51st IEEE Conf. Decis. Control (CDC) (2012) 5073–5078, https://doi.org/10.1109/CDC.2012.6426849.

[43] T. Ando, High-speed atomic force microscopy and its future prospects 10 285–292.

[44] A. Nievergelt, B. Erickson, N. Hosseini, J. Adams, G. Fantner, Studying biological membranes with extended range high-speed atomic force microscopy 5.10.1038/srep11987.

[45] F. Zuttion, A. Colom, S. Matile, D. Faragó, F. Pompeo, J. Kokavecz, A. Galinier, J. Sturgis, I. Casuso, High-speed atomic force microscopy highlights new molecular mechanism of daptomycin action 11.10.1038/s41467–020-19710-z.
[46] Mohammad, M. Coskun, Bulut, S. Moheimani, Reza, High dynamic range afm cantilever with a collocated piezoelectric actuator-sensor pair 29 (2) 260–267.10.1109/JMEMS.2020.2967794.
[47] L. Costa, M.S. Rodrigues, Influence of spurious resonances on the interaction force in dynamic afm, Beilstein Journal of Nanotechnology 6 (2015)420–427.10.3762/bjnano.6.42.
[48] S.I. Moore, M.G. Ruppert, Y.K. Yong, Multimodal cantilevers with novel piezoelectric layer topology for sensitivity enhancement, Beilstein J. Nanotechnol. 8 (2017) 358–371, https://doi.org/10.3762/bjnano.8.38.
[49] G.E. Fantner, D.J. Burns, A.M. Belcher, I.W. Rangelow, K. Youcef-Toumi, DMCMN: In Depth Characterization and Control of AFM Cantilevers With Integrated Sensing and Actuation, J. Dyn. Syst., Meas., Control 131 (6) (2009), 061104, https://doi.org/10.1115/1.4000378, 11, ⟨https://asmedigitalcollection.asme.org/dynamicsystems/article-pdf/131/6/061104/5782522/061104_1.pdf⟩.
[50] K. Ivanova, Y. Sarov, T. Ivanov, A. Frank, J. Zöllner, C. Bitterlich, U. Wenzel, B.E. Volland, S. Klett, I.W. Rangelow, P. Zawierucha, M. Zielony, T. Gotszalk, D. Dontzov, W. Schott, N. Nikolov, M. Zier, B. Schmidt, W. Engl, T. Sulzbach, I. Kostic, Scanning proximal probes for parallel imaging and lithography 26 (6) 2367–2373.10.1116/1.2990789.
[51] Y.M. Efremov, A.X. Cartagena-Rivera, A.I. M. Athamneh, D.M. Suter, A. Raman, Mapping heterogeneity of cellular mechanics by multi-harmonic atomic force microscopy 13 (10)2200–2216.10.1038/s41596–018-0031–8.
[52] J.D. Adams, P.L. T.M. Frederix, C.A. Bippes, Breakthrough instruments and products: DriveAFM for high-performance atomic force microscopy 92 (12) 129503.10.1063/5.0081190.
[53] A.S. Algamili, M.H. M. Khir, J.O. Dennis, A.Y. Ahmed, S.S. Alabsi, S.S. B. Hashwan, M.M. Junaid, A review of actuation and sensing mechanisms in MEMS-based sensor devices 16 (1). 10.1186/s11671–021-03481–7.
[54] S.W. Stahl, E.M. Puchner, H.E. Gaub, Photothermal cantilever actuation for fast single-molecule force spectroscopy (arXiv), Rev. Sci. Instrum. 80 (7) (2009), 073702, https://doi.org/10.1063/1.3157466 (arXiv), ⟨https://doi.org/10.1063/1.3157466⟩.
[55] D. Kiracofe, K. Kobayashi, A. Labuda, A. Raman, H. Yamada, High efficiency laser photothermal excitation of microcantilever vibrations in air and liquids, Rev. Sci. Instrum. 82 (2011), 013702, https://doi.org/10.1063/1.3518965.
[56] A.C. Hillier, A.J. Bard, ac-mode atomic force microscope imaging in air and solutions with a thermally driven bimetallic cantilever probe 68 (5) 2082–2090.10.1063/1.1148101.
[57] B. Sahu, C.R. Taylor, K.K. Leang, Emerging challenges of microactuators for nanoscale positioning, assembly, and manipulation 132 (3). 10.1115/1.4001662.
[58] A. Schemmel, H.E. Gaub, Single molecule force spectrometer with magnetic force control and inductive detection 70 (2)1313–1317.10.1063/1.1149590.
[59] B.O. Alunda, Y.J. Lee, Review: Cantilever-based sensors for high speed atomic force microscopy 20 (17)4784.10.3390/s20174784.
[60] M.B. Viani, T.E. Schäffer, A. Chand, M. Rief, H.E. Gaub, P.K. Hansma, Small cantilevers for force spectroscopy of single molecules (arXiv), J. Appl. Phys. 86 (4) (1999) 2258–2262, https://doi.org/10.1063/1.371039 (arXiv), ⟨https://doi.org/10.1063/1.371039⟩.
[61] R. Enning, D. Ziegler, A. Nievergelt, R. Friedlos, K. Venkataramani, A. Stemmer, A high frequency sensor for optical beam deflection atomic force microscopy (arXiv), Rev. Sci. Instrum. 82 (4) (2011), 043705, https://doi.org/10.1063/1.3575322 (arXiv), ⟨https://doi.org/10.1063/1.3575322⟩.
[62] C. Valotteau, F. Sumbul, F. Rico, High-speed force spectroscopy: microsecond force measurements using ultrashort cantilevers 11 (5)689–699.10.1007/s12551–019-00585–4.
[63] M.G. Ruppert, Y.K. Yong, Note: Guaranteed collocated multimode control of an atomic force microscope cantilever using on-chip piezoelectric actuation and sensing, Rev. Sci. Instrum. 88 (8) (2017), 086109, https://doi.org/10.1063/1.4990451 (arXiv), ⟨https://doi.org/10.1063/1.4990451⟩.
[64] M.B. Coskun, A.G. Fowler, M. Maroufi, S.O.R. Moheimani, On-chip feedthrough cancellation methods for microfabricated afm cantilevers with integrated piezoelectric transducers, J. Micro Syst. 26 (6) (2017) 1287–1297, https://doi.org/10.1109/JMEMS.2017.2731762.
[65] D. Lange, T. Akiyama, C. Hagleitner, A. Tonin, H. Hidber, P. Niedermann, U. Staufer, N. de Rooij, O. Brand, H. Baltes, Parallel scanning AFM with on-chip circuitry in CMOS technology, in: Technical Digest. International MEMS 99 Conference. Twelfth IEEE International Conference on Micro Electro Mechanical Systems (Cat. No.99CH36291), IEEE.10.1109/memsys.1999.746870.
[66] M.G. Ruppert, S.O.R. Moheimani, A novel self-sensing technique for tapping-mode atomic force microscopy (arXiv), Rev. Sci. Instrum. 84 (12) (2013), 125006, https://doi.org/10.1063/1.4841855 (arXiv), ⟨https://doi.org/10.1063/1.4841855⟩.
[67] Y.-S. Kim, H.-J. Nam, S.-M. Cho, J.-W. Hong, D.-C. Kim, J.U. Bu, Pzt cantilever array integrated with piezoresistor sensor for high speed parallel operation of afm, Sens. Actuators A: Phys. 103 (1) (2003) 122–129, https://doi.org/10.1016/S0924-4247(02)00311-4.
[68] T. Michels, E. Guliyev, M. Klukowski, I.W. Rangelow, Micromachined self-actuated piezoresistive cantilever for high speed spm, Microelectron. Eng. 97 (2012) 265–268, https://doi.org/10.1016/j.mee.2012.03.029, micro- and Nano-Engineering (MNE) 2011, selected contributions: Part I.
[69] S.O. RezaMoheimani, A. Fleming, Piezoelectric Transducers Vib. Control Damping (2006), https://doi.org/10.1007/1-84628-332-9.
[70] M. BulutCoskun, M. Baan, A. Alipour, S. O. Reza Moheimani, Design, fabrication, and characterization of a piezoelectric afm cantilever array, 2019 IEEE Conf. Control Technol. Appl. (CCTA) (2019) 227–232, https://doi.org/10.1109/CCTA.2019.8920686.
[71] A.G. Fowler, M.B. Coskun, S.O.R. Moheimani, Q control of a microfabricated piezoelectric cantilever with on-chip feedthrough cancellation. IEEE Conference on Control Technology and Applications (CCTA), IEEE,, 2017, https://doi.org/10.1109/ccta.2017.8062451.
[72] I.L. Guy, S. Muensit, E.M. Goldys, Extensional piezoelectric coefficients of gallium nitride and aluminum nitride 75 (26)4133–4135.10.1063/1.125560.
[73] R. Mahameed, N. Sinha, M.B. Pisani, G. Piazza, Dual-beam actuation of piezoelectric AlN RF MEMS switches monolithically integrated with AlN contour-mode resonators 18 (10) 105011.10.1088/0960–1317/18/10/105011.
[74] J. Sanchez-Rojas, J. Hernando, A. Ababneh, U. Schmid, J. Olivares, M. Clement, E. Iborra, Advanced determination of piezoelectric properties of AlN thin films on silicon substrates, IEEE.10.1109/ultsym.2008.0218.
[75] G. Piazza, V. Felmetsger, P. Muralt, R.H. O. III, R. Ruby, Piezoelectric aluminum nitride thin films for microelectromechanical systems 37 (11)1051–1061.10.1557/mrs.2012.268.
[76] S. Marauska, V. Hrkac, T. Dankwort, R. Jahns, H.J. Quenzer, R. Knöchel, L. Kienle, B. Wagner, Sputtered thin film piezoelectric aluminum nitride as a functional MEMS material 18 (6)787–795.10.1007/s00542–012-1493–1.
[77] G.K. Cowen A., Hames G., H. B., Piezomumps design handbook, Tech. rep., MEMSCAP Inc., 2014.
[78] H.J. Butt, M. Jaschke, Calculation of thermal noise in atomic force microscopy 6 (1)1–7.10.1088/0957–4484/6/1/001.

Natã Franco Soares de Bem graduated from Federal Center for Technological Education of Minas Gerais (CEFET/MG), Brazil, with a Bachelor of Control and Automation Engineering in 2018. He is currently a PhD student at the University of Newcastle, Australia. His research focus is on design, manufacturing, and microelectromechanical systems (MEMS).

Michael G. Ruppert received the Dipl.-Ing. degree in automation technology from the University of Stuttgart, Germany, in 2013 and the PhD degree in Electrical Engineering from The University of Newcastle, Australia in 2017. As a visiting researcher, he was with The University of Texas at Dallas, USA from 2015 until 2016 and he is currently a postdoctoral research fellow at The University of Newcastle. His research interests include the utilization of system theoretic tools for sensing, estimation and control in high-speed and multifrequency atomic force microscopy. Dr Ruppert's research has been recognized with the 2019 Best Conference Paper Award at the 2019 International Conference on Manipulation, Automation and Robotics at Small Scales (MARSS), the 2018 IEEE Transactions on Control Systems Technology Outstanding Paper Award, and the 2017 University of Newcastle Higher Degree by Research Excellence Award.

Andrew J. Fleming (M′02) received the B.Sc. degree in electrical engineering and the Ph.D. degree in mechatronics engineering from the University of Newcastle, Callaghan, NSW, Australia, in 2000 and 2004, respectively. He is currently an Australian Research Council Future Fellow and the Director with the Precision Mechatronics Lab, University of Newcastle. He is the co-author of three books, and more than 180 journal and conference articles. He is the Inventor of several patent applications. His research interests include lithography, nanopositioning, scanning probe microscopy, and biomedical devices. Dr. Fleming received the Academy for Technological Sciences and Engineering Baterham Medal in 2016, the Newcastle Innovation Rising Star Award for Excellence in Industrial Engagement in 2012, the IEEE Control Systems Society Outstanding Paper Award in 2007, and the University of Newcastle Researcher of the Year Award in 2007.

Yuen K. Yong received the Bachelor of Engineering degree in Mechatronics Engineering and the PhD degree in Mechanical Engineering from The University of Adelaide, Australia, in 2001 and 2007, respectively. She is current an associate professor at The University of Newcastle, Australia. Her research interests include nanopositioning systems, design and control of microcantilevers, atomic force microscopy, and miniature robotics. Dr Yong was an Australian Research Council DECRA fellow from 2013 to 2017. She is an associate editor for the IEEE/ASME Transactions of Mechatronics. She was the recipient of the University of Newcastle Vice-Chancellor's Award for Research Excellence in 2014 and the Vice-Chancellor's Award for Research Supervision Excellence in 2017.